UNDERGRADUATE THESIS DEFENSE FOR
DEPARTMENTAL HONORS
Department of Physics
Author: David Welsh
Infrared Vibrational Spectroscopy of Cold
Hydrocarbons

Committee Members:

Thesis Advisor: Prof. Heather Lewandowski, Department of Physics
Honor's Council Representative: Prof. John Cumalat, Department of Physics
Committee Member: Prof. Eric Thaler, Department of Applied Mathematics

Defense Date: 25 March 2019

Infrared Vibrational Spectroscopy of Cold Hydrocarbons

Author: David Welsh

Abstract

Infrared vibrational spectroscopy is a tool commonly used by physicists and chemists to study and identify chemical compounds. It exploits the fact that a molecule may absorb electromagnetic radiation that is characteristic to its structure, causing the bonds to stretch is some manner. This quantum mechanical phenomenon can be mathematically modeled, giving physicists a method to predict where these absorptions can occur. Vibrational spectroscopy can be used in conjunction with a buffer-gas molecular beam to create a cold, isolated matrix of inert molecules to trap a molecule of interest. Cold trapping a molecule in this manner, using a buffer gas cell, creates an ideal environment for vibrational spectroscopy, leading to high signal-to-noise ratios of a sample spectra.

While spectroscopic methods have been around for decades, the use of a molecular beam to form an isolated matrix is fairly new. With new methods in physics, it is important to look over molecules that have been well documented, especially when these molecules are important in energy, combustion, life, and organic chemistry. The molecules I am referring to are hydrocarbons, or long chains of carbon bonded with hydrogen. This experiment's purpose is to study hydrocarbons using vibrational infrared spectroscopy at extremely low temperatures trapped in an isolated matrix using a buffer gas cell. This will determine if using a buffer gas cell is a viable option to create higher order hydrocarbons and possibly the C-H radical, which is an important intermediate to many chemical bonds essential to life and energy.

Contents

List of Figures

1 Acknowledgments

This thesis constitutes the finale of a long, challenging undergraduate journey. This pipe-dream of an adventure was only possible because of my wife and children, who gave me motivation and encouragement to change careers. I also want to truly thank Professor Heather Lewandowski, who gave me the opportunity to work in an amazing field studying new and interesting physics. Professor Lewandowski's inspiring optimism is contagious and brings fresh life to the study of physics. I want to thank all the members of the Lewandowski group, who offered continual guidance and support during my time at the lab. I would not have succeeded without their knowledge in experimental physics, high pulse energy lasers, vacuum systems, and spectroscopy. I also want to thank my first mentor, Dr. Cameron Straatsma, who introduced me to the world of buffer gas beams and molecular spectroscopy. I would like to extend special gratitude to Professor Eric Thaler and Professor John Cumalat for sitting on the council and taking the time to review this thesis and sit in for the defense. Finally, I want to offer an appreciation to all the members of Physics Anonymous, who supported me in my endeavors.
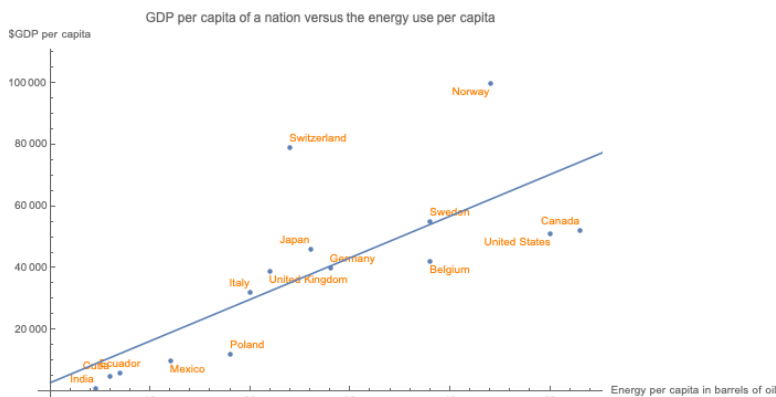
Figure 1: Graph depicting the Gross Domestic Product per capita against the amount of energy used per capita for various countries. The fitted linear curve shows a trend that an increase in energy correlates to an increase in $GDP per person. Adapted from [14, page 4]

.

2 Introduction

In the early 1700's, an innovative blacksmith named Thomas Newcomen developed a pump driven by steam, which was created from the burning of coal[7]. This was the first instance in history where the burning of a hydrocarbon, an organic molecule consisting only of carbon and hydrogen, was made to do work. Now, humanity relies more on hydrocarbons for energy needs than any other fuel source[14]. These hydrocarbons come in many types, and commonly used in the forms of methane (CH_4) for burning of natural gas, butane (C_4H_{10}) for lighters, propane (C_3H_8) for cooking, and higher alkanes and alkenes for gasoline.

It is no secret that the world faces an energy crisis. In 2012, over 700 million people in India went without power because suppliers could not keep up with demand [13]. In 2017, Austrailia faced severe energy shortages and blackouts due to outdated plants, extreme prices, and inefficiencies [10]. The continent of Africa, home to 1.2 billion people, faces the worst of these, where approximately two-thirds of the population, over 650 million people, go without reliable, consistent energy [6]. If one were to plot energy use against the Gross Domestic Product (GDP) of a nation, they would find a direct correlation between the energy used by a nation and the GDP per capita[14]. One could argue that this shows a trend that the energy used per person could relate to the quality of life that person receives. A depiction of this can be seen in Figure 1. Because of this, it is essential to study hydrocarbons, our greatest source of fuel, specifically the simplest ingredients of it: the carbon-hydrogen chemical bond.

2.1 Purpose and Objective of Experiment

The purpose and goals of my experiment are to conduct infrared vibrational spectroscopy on an ablated carbon and hydrogen source inside a buffer gas cell to observe a trapped hydrocarbon or the C-H radical (methylidyne) in an isolated matrix. Spectroscopy of this kind, using a buffer gas sourced molecular beam, has rarely been done on higher order molecules, especially organic molecules like hydrocarbons. In doing so, this experiment, or others that follow it, could gain insight to energy and combustion processes or the formation of protocells that could answer questions about the origin of life.

This experiment has three main objectives and outcomes. First, conduct a simulation of the buffer gas cell used for the experimental process. This characterizes the device and sheds light on which parameters maximize signal. The second is the recreation of a carbon cluster experiment conducted by Dr. Cameron Straatsma in 2017. This part will help confirm carbon cluster vibrational modes and ensure the experimental apparatus is properly set up. Finally, the last experimental objective is the study of hydrocarbons with infrared vibrational spectroscopy using a buffer gas beam and matrix isolation. This study will be used to determine how viable the buffer gas cell is in creating hydrocarbons and the C-H radical and what parameters are needed in the hydrocarbon's formation.

2.2 Introduction to Methylidyne (C-H)

The C-H radical, also known as methylidyne, is the simplest component of hydrocarbons and other organic molecules. This molecule consists of a single carbon bonded with hydrogen and three unpaired electrons in the outer shell. It is highly unstable because of this, and therefore considered extremely reactive, which makes it difficult to study. Since reactions can occur on the order of nanoseconds, the experimentalist must either observe C-H very fast or slow the reactions down in order to study it. Attempting to observe this radical on these timescales is difficult, so a good method is to cool the molecules to a few kelvin and isolate them, where the reactions slow and simplify and the electronic states tend to reduce to the ground state. While the C-H radical has been well characterized in other experiments using spectroscopy, there are no documented results of observing and studying methylidyne using a buffer gas beam source and a rare gas matrix. A buffer gas beam can cool a gaseous mixture of carbon, hydrogen, and an inert gas to a few kelvin temperatures. Freezing it into an isolated matrix allows one to study the radical in an inert environment.

3 Background

3.1 Spectroscopy

Spectroscopy is a tool commonly used by physicists and chemists to study and identify molecules. To understand the more complex molecular spectroscopy, it is important first to grasp the fundamental concepts of the atomic structure and the spectra that arises from it. The simplest form of spectroscopy, and where it originated from, is the observation of the atomic spectra of hydrogen. This spectra arises from the electron transitioning between electronic energy levels. If electromagnetic radiation is absorbed, the electron will transition to a higher energy state. However, if the electron transitions to a lower energy state, the excess energy is emmitted as light.[2]. This energy can be predicted using the Rydberg Formula:

$$\Delta E = hcR_H(\frac{1}{n_1^2} - \frac{1}{n_2^2}) \qquad (3.1.1)$$

Where h is Planck's constant, c is the speed of light, R_H is the Rydberg constant for hydrogen, and n is the quantum number used to label the quantum states of energies[8]. Since energy is conserved, the energy that is released as radiation is carried away as a photon. Using and manipulating equation (3.1.1), the frequency of the photon released can be determined as $\nu = \frac{\Delta E}{h}$. However, in spectroscopy, it is common to use wavenumbers to measure frequency, where a wavenumber is the number of wavelengths per centimeter or cm^{-1}. To convert frequency to wavenumber, one simply takes the inverse of the wavelength in centimeters, $\tilde{\nu} = \frac{1}{\lambda}$. A simple manipulation of equation (3.1.1) gives the predicted transition energies in terms of the wavenumber of the photon that is emitted or absorbed.

$$\tilde{\nu} = \frac{\Delta E}{hc} = R_H(\frac{1}{n_1^2} - \frac{1}{n_2^2}) \qquad (3.1.2)$$

3.1.1 Molecular Spectroscopy

Molecules are slightly more complex than their fundamental building blocks, but the foundation is the same. With atoms, we simply looked at the changes in the electronic quantum number to determine the quantum states of energies, or their electronic transitions. However, molecular spectra arise from electronic, vibrational, and rotational transitions [2]. In most cases, the energy involved in rotational transitions is much less than those of vibrational transitions, which in turn are less than electronic transitions. This can be depicted visually in Figure 2, where the rotational energy states are set between each vibrational state, and vibrational transitions occur between different levels of the same energy state[8].
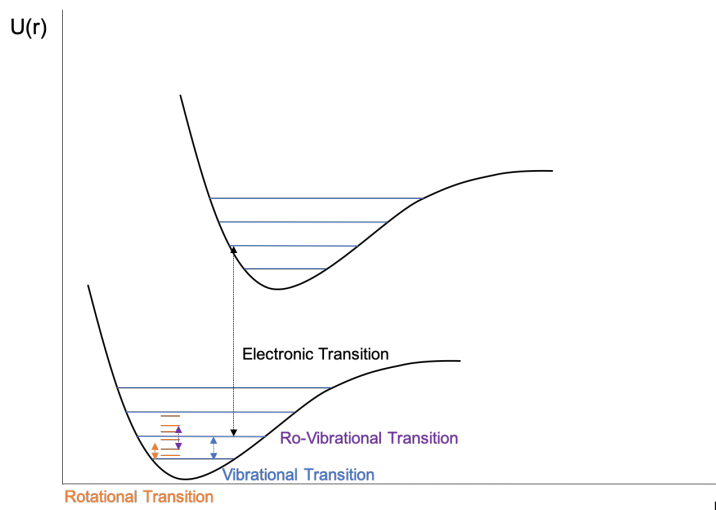
Figure 2: Visual depiction of the energy transitions in the form of electronic, vibrational, and rotational states. Adapted from [8, page 307].

3.1.2 Rotational Transitions

The rotational energies of molecules can be thought of in the classical sense as rigid rotors rotating about a central axis in three dimensions. The rotation gives rise to kinetic energy, which is used to determine the Hamiltonian of the system and the overall energy levels. Still considering the classical mechanical concepts of a rigid body, the total kinetic energy due to the rotation is

$$T = \frac{1}{2}I_{xx}\omega_x^2 + \frac{1}{2}I_{yy}\omega_y^2 + \frac{1}{2}I_{zz}\omega_z^2 \qquad (3.1.3)$$

For a more compact form, we can introduce the variable J to substitute in for the classical expression of the moment of inertia, $J_i = I_{ii}\omega_i$, and the expression reduces to

$$T = \frac{J_x^2}{2I_{xx}} + \frac{J_y^2}{2I_{yy}} + \frac{J_z^2}{2I_{zz}} \qquad (3.1.4)$$

Molecules frequently have identical moments of inertia in two dimensions. In this case, $I_{xx} = I_{yy} = I_\perp$ and the Hamiltonian reduces to the following expression:

$$\hat{H} = \frac{1}{2I_\perp}\hat{J}^2 + \left(\frac{1}{2I_{zz}} - \frac{1}{2I_\perp}\right)\hat{J}_z^2 \qquad (3.1.5)$$

Here, we transitioned from a classical sense to the quantum level by introducing operators. In equation (3.1.5), $\hat{J}^2$ is the total angular momentum operator and $\hat{J}_z$ is the projection of the momentum onto the $\hat{z}$ axis. This choice of operator

is convenient because it simultaneously is diagonalizable. The orthogonal solutions are called spherical harmonics. In systems of spherical harmonics, total angular momentum operators have eigenvalues $l(l + 1)\hbar^2$ and the z-component has eigenvalues $m\hbar$. We can relate this to the Hamiltonian of the rotational states as $J(J + 1)\hbar^2$ (where J is an integer 0,1,2,...) and $K\hbar$, using K in place of m ($K = J, J - 1$) for angular momentum about the principle axis. Using this, the energy levels for a rotational transition of a symmetric molecule becomes

$$E = \frac{\hbar^2}{2I_\perp}J(J + 1) + (\frac{\hbar^2}{2I_{zz}} - \frac{\hbar^2}{2I_\perp})K^2 \qquad (3.1.6)$$

Here, it is convention to define constants A and B, which are called the Rotation Constants, to put the energies in terms of wavenumbers.

$$A = \frac{\hbar}{4\pi c I_{zz}}, B = \frac{\hbar}{4\pi c I_\perp} \qquad (3.1.7)$$

Which gives a more convenient form for the energy as

$$\frac{E}{hc} = BJ(J + 1) + (A - B)K^2 \qquad (3.1.8)$$

Knowing the energy level of various rotational levels allow us to solve for the transition energy. With the known energy level, the energy of an emitted or absorbed photon becomes

$$\tilde{\nu} = \frac{E_{J+1} - E_J}{hc} = 2B(J + 1) \qquad (3.1.9)$$

Equation (3.1.9) tells us it is possible to predict the frequency of the electromagnetic radiation that is absorbed or emitted with a change in rotational energy.

3.1.3 Vibrational Transitions

Vibrational transitions arise when the nuclei of molecules are disturbed from their equilbrium position[2]. It is easy to picture this if you compare the bond of a diatomic molecule to a spring, then classically it looks like masses attached to a spring, as depicted in Figure 3.

If the spring is stretched or compressed it will gain and store energy. Because of this, it is best to mathematically describe this system as a simple harmonic oscillator with small displacements [2]. From classical mechanics, the restoring force of a harmonic oscillator is $F_{restore} = -kx$[16], where k is the force constant of proportionality. Since force is the negative gradient of the potential, $F = -\nabla V$, the potential energy of a harmonic oscillator is

$$V(x) = \frac{1}{2}kx^2 \qquad (3.1.10)$$

Equation 3.1.10 tells us this potential can be modeled as a well in the shape of a parabola, shown in figure 4. The total mechanical energy, the potential and
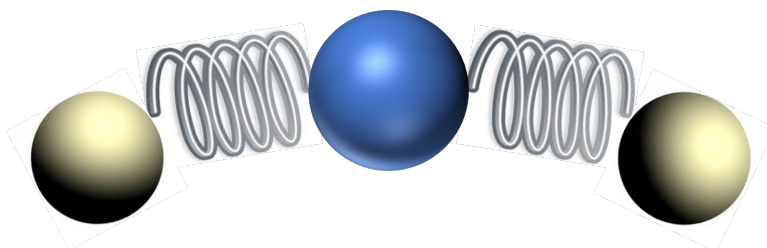
Figure 3: Classical depiction of a simple harmonic oscillator (SHO), which can be used to describe the vibrations of a molecule in a classical sense.

$E_3 = \dfrac{7\hbar\omega}{2}$

$E_2 = \dfrac{5\hbar\omega}{2}$

$E_1 = \dfrac{3\hbar\omega}{2}$

$E_0 = \dfrac{\hbar\omega}{2}$
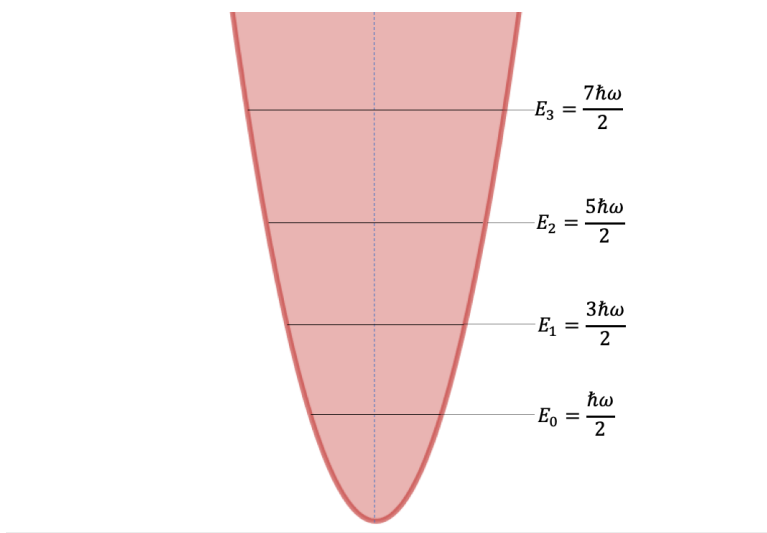
Figure 4: Potential well of a simple harmonic oscillator with changes of energy given as $\hbar\omega$.

kinetic, of this system can be described as

$$E = \frac{p^2}{2m} + \frac{1}{2}kx^2 \qquad (3.1.11)$$

Now we change the momentum and position, p and x, to operators, $\hat{p}$ and $\hat{x}$, and defining $\omega = \sqrt{\frac{k}{m}}$, the energy, or the Hamiltonian operator, becomes

$$\hat{H} = \frac{\hat{p^2}}{2m} + \frac{1}{2}m\omega^2\hat{x}^2 \qquad (3.1.12)$$

Using position space as the common basis, $\hat{p} = -i\hbar\frac{d}{dx}$ and our Hamiltonian from equation 3.1.12 simplifies to

$$H = \frac{-\hbar^2}{2m}\frac{d^2}{dx^2} + \frac{1}{2}kx^2 \qquad (3.1.13)$$

Which gives rise to the Schrödinger equation for the system.

$$E\Psi = \frac{-\hbar^2}{2m}\frac{d^2\Psi}{dx^2} + \frac{1}{2}kx^2\Psi \qquad (3.1.14)$$

This differential equation can be solved via brute force, but over the years physicists and mathematicians have developed a more elegant way to solve it: raising and lowering operators. We can define two operators $a = \sqrt{\frac{mw}{2\hbar}}(\hat{x}+i\frac{\hat{p}}{mw})$ and its complex conjugate transpose, $a^\dagger = \sqrt{\frac{mw}{2\hbar}}(\hat{x} - i\frac{\hat{p}}{mw})$. Using these two operators, the Hamiltonian can be expressed as

$$H = \hbar\omega(a^\dagger a + \frac{1}{2}) \qquad (3.1.15)$$

Finally, using the Hamiltonian to solve the energy eigenvalue equation gives the expected energy spectrum of the system,

$$E_\nu = \hbar\omega(\nu + \frac{1}{2}) \qquad (3.1.16)$$

where ν is the vibrational quantum level. Now, to correctly model a diatomic molecule as a harmonic oscillator, the mass of the system is not simply m, but the reduced mass $\mu = \frac{m_a m_b}{m_a+m_b}$. Note that the Energy levels change slightly due to the change of the fundamental frequency ω, defined as

$$\omega = \sqrt{\frac{k}{\mu}} \qquad (3.1.17)$$

To predict the spectrum absorbed, electric dipole selection rules must be implemented. The probability for a system to make a transition, such as a vibrational energy state raising or lowering by an $\hbar\ \omega$, is proportional to the matrix element of the interaction between the two states. If the bound system has some charge given by q, then the matrix element in this case is given as

14

$\langle \tilde{\nu}|q\hat{x}|\nu\rangle$. Because this matrix element position only connects adjacent states, then the elements will vanish unless $\tilde{\nu} = \nu \pm 1$, or

$$\langle \tilde{\nu}|q\hat{x}|\nu\rangle = \delta_{\tilde{\nu},\nu} \pm 1 \qquad (3.1.18)$$

So, this can be shown that the selection rule for a harmonic oscillator is

$$\Delta\nu = \tilde{\nu} - \nu = \pm 1 \qquad (3.1.19)$$

From this, we can determine the vibrational absorptions will occur at wavenumbers given by

$$\tilde{\nu} = \frac{E_{\nu+1} - E_\nu}{hc} = \frac{\hbar\omega}{hc} = \frac{\omega}{2\pi c} = \frac{1}{2\pi c}\sqrt{\frac{k}{\mu}} \qquad (3.1.20)$$

So, using equation (3.1.20), we can accurately predict the absorption of electromagnetic radiation based on the reduced mass of a molecule due to the vibrations of the bonds. However, recall that many assumptions were made to get to this equation, and while it is accurate with a proper k number, it is not perfect. We modeled the system as a perfect simple harmonic oscillator however, observation shows that the energy levels are expected to converge as the quantum number increases. The actual potential is given in Figure 5, overlaid on the harmonic approximation to show the differences. The reason the actual potential (shown in green in Figure 5) diverges in this manner is due to the Coulomb force, expressed as

$$F = k_e \frac{q_1 q_2}{r^2} \qquad (3.1.21)$$

which tells us that the atoms between bonds can be separated by a distance r, with charges q_1 and q_2. k_e in Equation 3.1.21 is a constant, approximately $9*10^9 Nm^2 C^{-2}$. If r where to get very large, the force between the atoms would go to zero. Intuitively this makes sense, if the atoms were to get very far they would not affect one another and the bonds would simply break. However, as the atoms get closer together, r gets very small and the force becomes infinitely large, causing the atoms to repel one another. This offers the explanation as to why the potentials in Figure 5 are different. However, for this experiment, the approximation of the potential given by the simple harmonic oscillator shown in red in Figure 5 is quite adequate, and is used instead of the actual potential.

3.1.4 Absorption Spectroscopy

When light passes through a sample molecule, there is a chance that the electromagnetic radiation could be absorbed, which causes the molecule to change energy states. This depends on the frequency of light, the molecule itself, and the state the molecule is currently in. This method is commonly used to identify molecules and can be plotted on a graph of wavenumber of electromagnetic radiation versus absorbance. Absorbance is a unitless quantity that is the ratio of
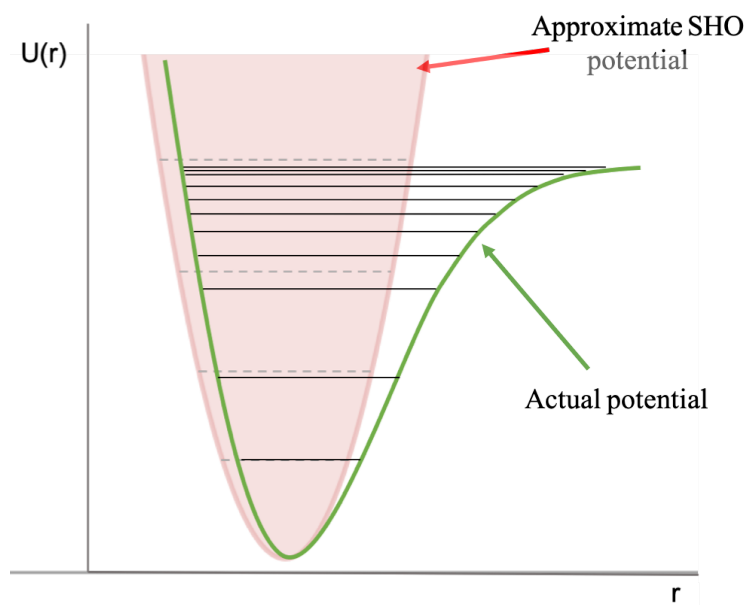
Figure 5: Actual potential versus the simple harmonic oscillator (SHO) showing vibrational energy levels. In this depiction, the SHO, used as an approximation, is depicted in red while the actual absorption is depicted in green.
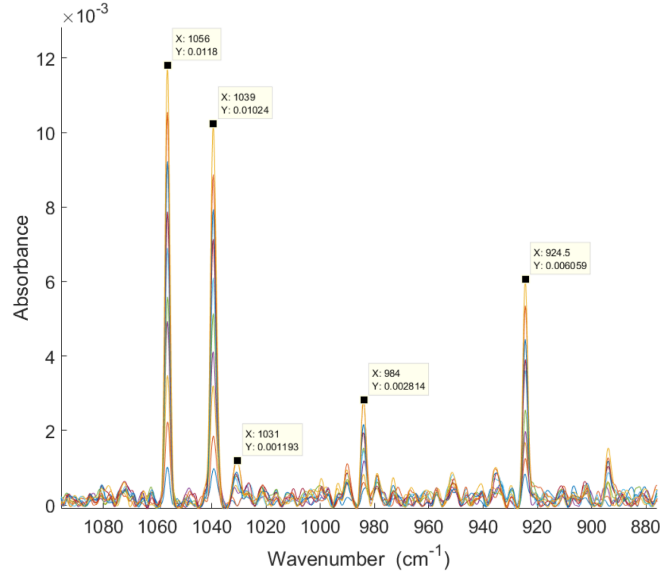
Figure 6: Sample image of an absorption spectrum that shows vibrational modes of a molecule by the absorbance given at a specific wavenumber of electromagnetic radiation

the incident to transmitted flux of light in a log-base-ten value[9]. It is described mathematically by the following equation.

$$A = -log_{10}(\frac{\Phi_T}{\Phi_I})$$
(3.1.22)

where Φ_T is the flux of transmitted light and Φ_I is the flux of incident light. Alternatively, instead of absorbance, the transmitted light could instead be measured in optical depth, τ. Optical depth is the ratio of the natural log of the incident to transmitted light[9] and is also dimensionless.

$$\tau = ln(\frac{\Phi_I}{\Phi_T})$$
(3.1.23)

While equation 3.1.23 is useful in many situations, it could also be described in terms of the Beer-Lambert Law. This law states that optical depth is proportional to the number density of the material n, the attenuation cross section σ, and the length which the electromagnetic radiation passes through, l.

$$\tau = \sigma n l$$
(3.1.24)

A sample image of an absorption spectrum is given in Figure 6, and it shows wavenumbers along the x-axis and absorbance along the y-axis.
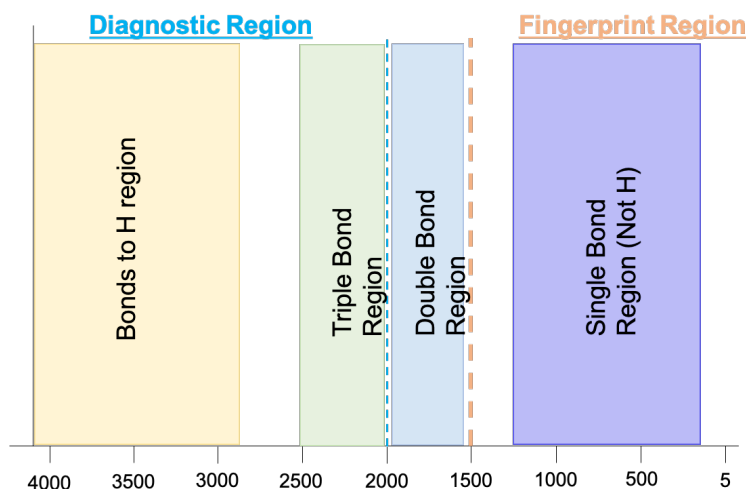
Figure 7: A depiction of helpful guidelines for absorption spectroscopy broken into two categories: The Diagnostic region and the fingerprint region. This is then subdivided into areas with common bonds. The x-axis depicts the location of the spectrum in wavenumbers.

In Figure 6, when absorption is near 0, all of the light is able to pass through the molecule, and none is absorbed as a vibrational, rotational, or electronic transition. However, at very specific wavenumbers, characteristic to the molecule's structure, the light is absorbed creating a change in energy, which we see as peaks above the noise floor.

There are common rules of thumb that physicists and chemists use when conducting absorption spectroscopy. Specifically, there are two common regions on a graph that help scientists identify molecules called the diagnostic region and the fingerprint region. The diagnostic region tends to fall on higher wavenumbers, greater than $2000 cm^{-1}$, and the fingerprint region usually falls below $1500 cm^{-1}$. The diagnostic region helps scientists narrow down what molecules could be in the sample, while the fingerprint region commonly helps pinpoint specific molecules in question. On top of this, there are other helpful guides that, while not always correct, could help narrow down the molecule that is absorbing light. The helpful guidelines are neatly organized in Figure 7.

3.1.5 Fourier Transform Infrared Spectrometer (FTIR)

To physically excite molecules for vibrational spectroscopy, an infrared beam needs to pass through the sample before it is analyzed. To do this, I made use of an FTIR, or Fourier Transform Infrared Spectrometer. Many FTIR devices mimic the design of the Michelson-Morley interferometer, which incorportates a light beam, a beam splitter, a fixed mirror, a movable mirror, and a detector

18
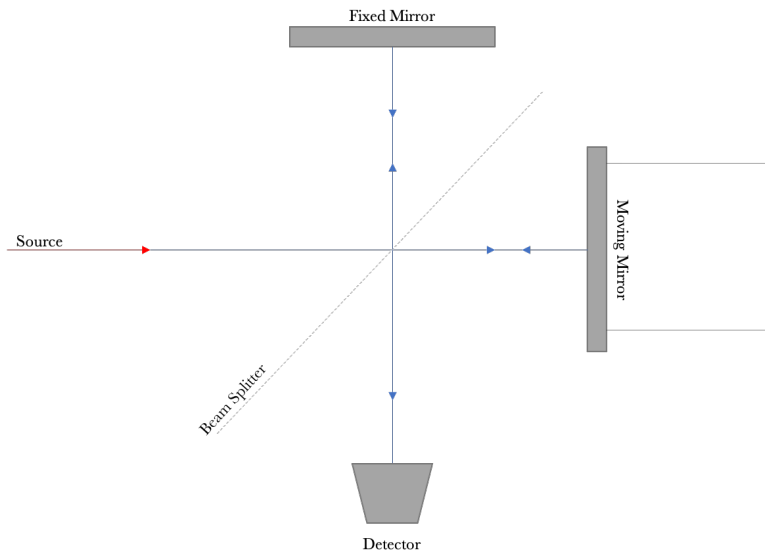
Figure 8: A Michelson-Morley Interferometer, which is the basic design of an FTIR. Adapted from [4].

[4]. The light beam is first divided into two paths, then recombined after a path difference is introduced [4]. This creates a condition in which interference between the beams can occur. An example of this can be seen in Figure 8.

When the beam leaves the source, it first interacts with the beam splitter. This allows partial reflectance and transmittance, and divides the beam into two paths. One path travels to the fixed mirror while the second, $90 \deg$ off from the first, proceeds to the moving mirror. The distance between the two is known as the optical path difference. The beams reflect off their respective mirrors, then return to the beam splitter where they interact with one another then reflect and transmit again. The transmitted beam, as shown in Figure 8, returns to the source while the reflected beam moves on to the detector.

The moving mirror can traverse along its path in two ways, either with a constant velocity, called a continuous-scan interferometer, or via small steps over a short period, denoted as a step-scan interferometer [4]. To best describe the functionality of the interferometer, I will refer to the step-scan version first. When the moving mirror takes a discrete step, the light travels two times the optical path difference and a distance, δ, called the retardation [4]. When δ is zero, the mirrors are equal distant apart. After striking the mirrors, when the beams join together at the splitter again, their frequencies create constructive interference. In this case, all the light reaches the detector and none travels to the source. If however the moving mirror takes a discrete step to a distance of one-quarter of a wavelength, $\frac{\lambda}{4}$, then the total retardation is $\frac{\lambda}{2}$, or half the wavelength. In this case, when the beams rejoin at the splitter, they are com-

Interferogram

Fourier Transform

Spectrum
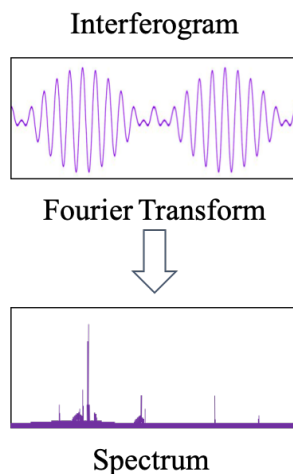
Figure 9: Image depicting the resulting interferogram from constructive and destructive interference due to a moving mirror. A Fast Fourier Transform is applied to the interferogram changing it from a function of position based on the moving mirror to a function of wavenumber, giving a spectrum.

pletely out of phase with one another and interfere destructively. All of the light travels back to the source with nothing going to the detector. This pattern could continue as the moving mirror migrates another $\frac{\lambda}{4}$, then $\delta = \lambda$, and the frequencies are back in phase. This continuous change in the retardation develops an interferogram of the infrared electromagnetic radiation, which can be seen in Figure 9.

When these variations of intensity are monitored as a function of the path-length difference, we can record and act a Fast Fourier Transform on the interferogram to find the intensity of the source as a function of wavenumber [4]. Before a molecular sample is added to the interferogram, a background spectral image is taken. Once a sample is added between the detector and the output the molecules will absorb some of the infrared electromagnetic radiation at specific wavenumbers, causing an alteration in the interferogram. After the Fast Fourier Transform is applied, the resulting spectrum is ratioed with the background scan, resulting in only the absorbance spikes created by the excitation of the source at the specific wavenumber. The FTIR generally takes a multitude of scans, then averages the resulting spectrum to clean the signal. This resulting spectrum offers physicists and chemists the ability to physically see where absorptions take place and with what intensities based on the molecular sample.
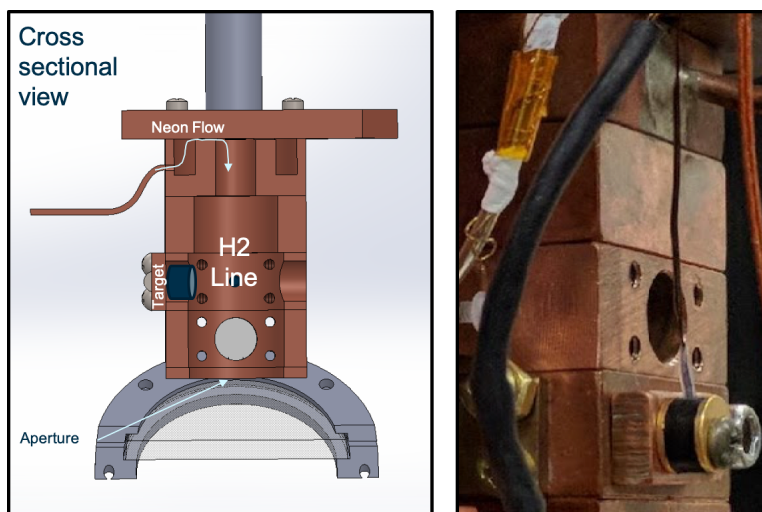
Figure 10: Cutout view of the buffer gas cell showing neon flow path and a photographic depiction of the actual buffer gas cell used for my research.

3.2 Buffer Gas Cell

A buffer gas cell is a small, cold chamber designed to mix molecular sources with inert gases which can later be studied using spectroscopy. The inert gas, also called the buffer gas, is mixed with a molecule of interest, also in gas phase, then forced out of a small aperture at the bottom of the cell. This mixture is called the buffer gas beam and can either be probed in this gas phase or frozen in a matrix and studied as a solid.

3.2.1 Cell Geometry

The buffer gas cell is typically small and housed inside a cryogenic chamber for cooling purposes. The buffer gas cell used in my experiment has dimensions of 53mm tall, 31.5mm wide, and 31.5mm long, with an aperture size of 5mm. The figure below shows a cutout view of the buffer gas cell, along with the flow of the buffer gas, neon. The buffer gas enters from a tube in the top then flows into a secondary, holding chamber to help equalize the flow into the main cell. Next, the buffer gas is forced into the main cell where it will interact with the molecular source of interest. Finally, the buffer gas along with the source is forced out of the cell through the aperture at the bottom where it can be sampled.
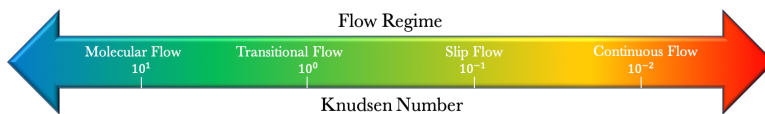
Figure 11: Depiction of the Knudsen numbers with the corresponding flow regime

3.2.2 Fluid Dynamics

Fluid dynamics studies the mechanics of how gases and liquids flow and move. Depending on a specific set of parameters, this sub-discipline can be studied and modeled by looking at the fluid as a continuous, flowing mass, as individual molecules interacting with their environment, or regimes between these two. To determine how your system behaves along this spectrum, it is important to define and understand the Knudsen number. The Knudsen number is a unitless measurement that describes the molecular flow of a system, and given as

$$K_n = \frac{\lambda}{l} \tag{3.2.1}$$

where λ is the mean free path, or the average distance traveled by a moving particle before a collision, and l is the length of the confined region. If you assume ideal gas law, the Knudsen number can instead be calculated using the Boltzman constant, k_B, the kinetic diameter of the molecule, d, and the pressure of the system, p.

$$K_n = \frac{k_B T}{\sqrt{2}\pi d^2 p l} \tag{3.2.2}$$

The flow regimes are generally broken into four pillars, traversing from continuum to statistical models as follows: Continuous flow ($K_n < 0.01$), Slip flow ($K_n < 0.1$), Transitional flow ($K_n < 10$), and Free Molecular flow ($K_n > 10$) [15]. A visual depiction of this can be seen in Figure 11.

As expected, Continuous Flow arises from areas of high pressure, while Free Molecular Flow is found in vacuum. An example of a system with a very low Knudsen number would be water moving through a pipe, where as the regions in interstellar space would be expressed with high Knudsen numbers. Figure 12 shows a logarithmic plot of mean free path versus the length for fixed Knudsen numbers. This shows the trend that the larger the distance between molecular collisions, and the larger the system's confined region, the Knudsen number will increase. Based on the parameters for neon's mean free path, and the system I use for my experiment is high vacuum, the Knudsen number I work work is approximately 10. This means any physical model of this system must be done in a free-molecular regime to offer insights into the fluid dynamics and mechanics. Figure 12 gives a red box, indicating the approximated regime where my system fits, based on λ and l.
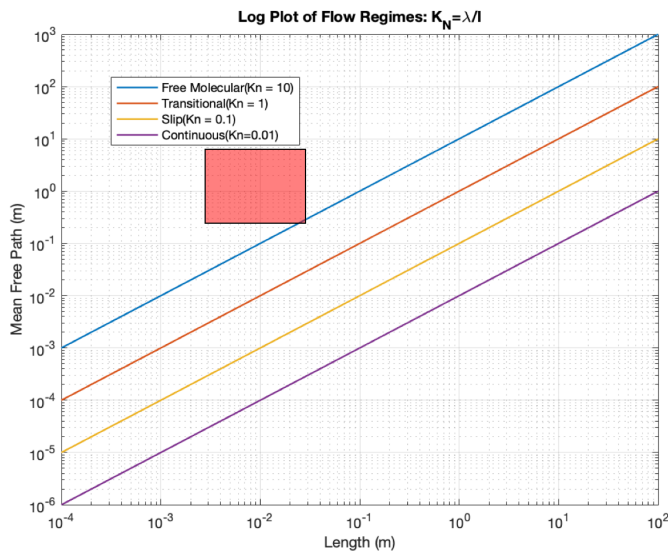
Figure 12: Plot of mean free path vs. length for fixed Knudsen numbers. The red box indicates the regime where my system falls based on the mean free path λ and the length of the region l. For simulation purposes, it can be approximated to a Knudsen number of 10.

3.3 Matrix Isolation

Matrix isolation is the method in which guest molecules are trapped in a rigid host of materials and prevented from undergoing diffusion[12]. A matrix allows the experimentalist to study molecular vibrational modes without exciting rotational transitions. Because of this, matrix isolation methods show a spectrum with high, sharp peaks, which allows for greater accuracy when seeking molecules of interest [12].

The buffer gas cell is one method used to create a matrix. In the buffer gas cell an inert gas, or buffer gas, mixes with the guest molecules, which are the molecules the experimentalist intends to study. This mixture is forced out of the aperture in the bottom of the cell as a molecular beam, where it is frozen on a window below. Figure ?? shows the glass window located directly beneath the aperture of the Buffer Gas Cell where the matrix forms. When frozen in the isolated matrix, the molecular beam's rotations are suppressed; however, it still has the freedom to vibrate and stretch chemical bonds when absorbing infrared light. Using this method, we can strictly perform vibrational spectroscopy without worrying about exciting rotational energies. A depiction of matrix isolation can be seen in Figure 13.

Matrix isolation for vibrational spectroscopy does have disadvantages that must be understood to accurately perform an experiment. One instance is
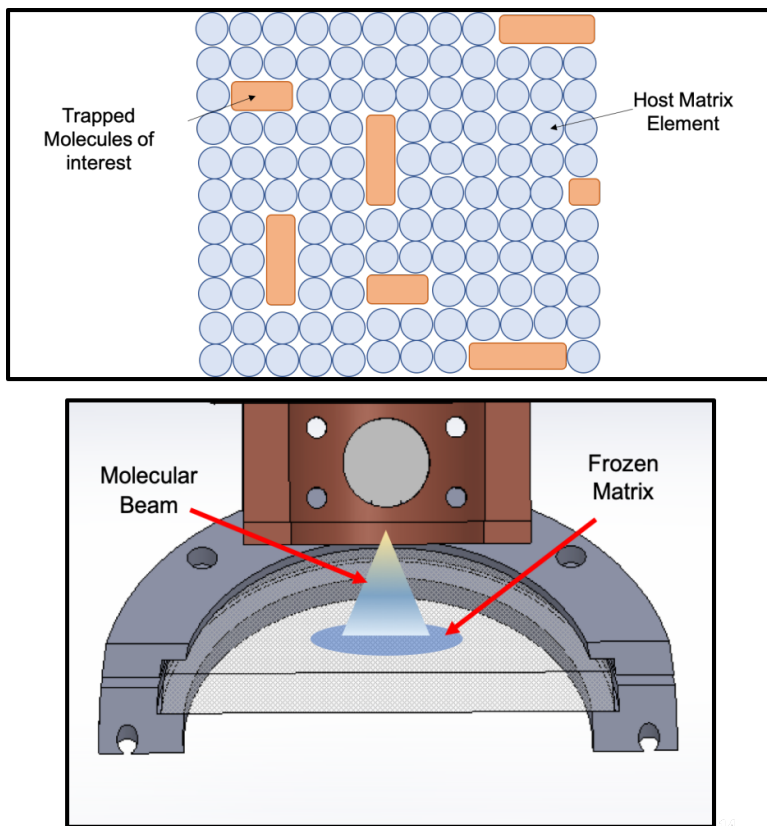
Figure 13: Image showing how a molecule of interest is isolated inside a host matrix and a cross-sectional depiction of the buffer gas cell creating a matrix from a buffer gas beam.

the possible shifting of frequencies of the normal modes of molecules. This occurs either through the electronic field of the buffer gas (host) material used, or through the effective increase of a force constant when atoms must work against the rigid, matrix environment[12]. It also changes with the choice of inert gas. Matrix shifts in neon appear to be the smallest, and the shifts tend to increase with an increase in mass of the host gas[1]. Shifts towards the longer wavelength region, also known as red-shifting, is more common than shorter regions, or blue-shifting. Also, when conducting vibrational spectroscopy on the unpaired electrons typical of radicals, it is possible to experience large deviations of molecular vibrational modes[1]. These inconsistencies must be noted by the experimentalist when preforming matrix isolation techniques to better evaluate data.

4 Methods

4.1 Experimental Setup

4.1.1 The Cryogenic System - Assembly and Disassembly

Often times, the experimental apparatus will need mechanical maintenance. For example, the matrix deposition on the window will need to be manually cleaned, or the target replaced. To do this, one needs to open the cryogenic chamber while the system is at room temperature and atmospheric pressure. The entire experimental apparatus is housed inside a cryogenic vacuum. The exterior of the system is mostly made up of stainless steel ConFlat (CF) flanges secured together with CF bolts. When the system is not under vacuum, it can be disassembled at the joint just below the bypass roughing valve, which is secured by 20, 5/16" CF bolts, each labeled. To easily separate the lower half of the system from the upper, a small hydraulic lift can be utilized to gently lower the bottom half of the system after the bolts have been removed. Directly beneath this outer housing is the radiation shield, which is held in place via six hex bolts. Once these are removed, the entire shield can be lowered into the bottom half of the cryogenic system, which exposes the buffer gas cell and the second stage of the cryogenic system. To reassemble the system, simply follow the instructions in the reverse order, ensuring that the CF bolts are tightened in ascending, numerical order.

4.1.2 Cooling the System and Pumping Down

Before conducting an experiment, the system needs to pump down the pressure and cool it to near absolute temperatures. The following steps outline the procedures for this:

1. Open the bypass roughing valve. This valve allows the scroll pump to bypass the turbo in the initial pumping phase.

2. Ensure the gas line valves are closed to both hydrogen and neon, and the gas line to the rough is closed.

3. Turn on the scroll (rough) pump, then slowly open the main roughing valve. The primary MKS pressure gauge should read at 100 mTorr after five minutes of pumping.

4. Allow the system to rough for one to two hours. The primary MKS gauge should read 35 mTorr before continuing.

5. Close the bypass roughing valve and turn on the turbo by pressing the button labeled "Start" on the Varian Turbo-V 70 device and allow the system to run for approximately 30 minutes.

6. Turn on the ion gauge by pressing the "gauge" reset switch on the P330 Ionization Gauge Controller.

7. Allow the system to pump down to $1 * 10^{-6}$ Torr before continuing.

8. In the maintenance hallway locate the cryogenic water supply and return manifold, labeled "cryo comp. supply" and "cryo comp. return" respectively. Turn both values perpendicular to the manifold to open.

9. Turn the cryogenic system on, located in the same service corridor as the water manifold, by turning the master switch clockwise, then pressing the "ON" button.

10. The system should stabilize overnight at a pressure of approximately $1 * 10^{-8}$ Torr with a window temperature of $5.5K$.

To warm the system up for maintenance, turn the Turbo pump off first by pressing the "stop" button on the controller. Allow the turbo to spin down for approximately 45 minutes, then turn the cryo-system off and follow the above procedures in the reverse order.

4.1.3 LabView and OMNIC Software

The experiment relies on two main software programs to run: Labview and OMNIC. The Labview code runs the experiment and displays important data analytics like the temperature and pressure of the system in an easy to use Graphical User Interface (GUI). It is also used to set the parameters of the experiment. OMNIC is the software program that operates the FTIR. The Labview code is setup specifically to interact with OMNIC to be as user friendly as possible.

Labview   The Labview program can be found in the following folder: c:\ Users\LewanLab \Desktop\Chaos Control System\Automated Spectrum Collection\Main.vi. After the program is opened, the main display will look like the image presented in Figure 14
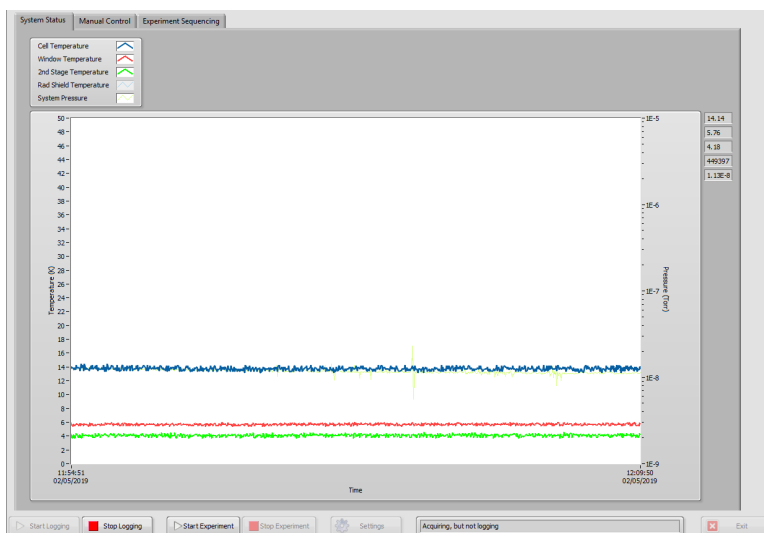
Figure 14: Main display of Labview program which runs experiment. Each thick line indicates the temperature at a specific location inside the chamber, where blue is the buffer gas cell, green is the second stage cryo, and red is the window. The light green line gives the system pressure in torr. The x axis is time, the y-left axis is temperature in Kelvin, and the y-right axis is pressure in torr.

In Figure 14, each thickly colored line depicts temperature data from a different point in the chamber. Blue shows the temperture of the buffer gas cell, green is the second-stage of the cryosystem, and red is the window. The light green line represents the pressure of the system, which is read from an ion gauge. To begin the logging process, simply press the "start logging" button on the lower left. To vary the range of either the temperature or pressure, click on the desired axis and manually type the preferred range. To set up an experiment, click on the third tab titled, "Experimental Sequencing." This tab will bring the user to a window that is shown in figure 15.

This window allows the user to manually input a number of parameters that effect the outcome of the experiment and controls the temperature ramp for cleaning the window. The first parameter the user can change is the number of samples to collect. This input, located in the top left, is the number of cycles the experiment will run, which allows the sample to accumulate and grow in a linear fashion. The deposition time sets the time in seconds that the ablation will occur. Finally, the flow rate command sets the flow rate for Neon in standard cubic centimeters per minute (*sccm*). This command takes an input "AS⟨flowrate⟩", which is the standard command for the Alicat Mass Flow Controller. Some good default parameters to consider are the following:

1. **Number of Sample Spectra** 15
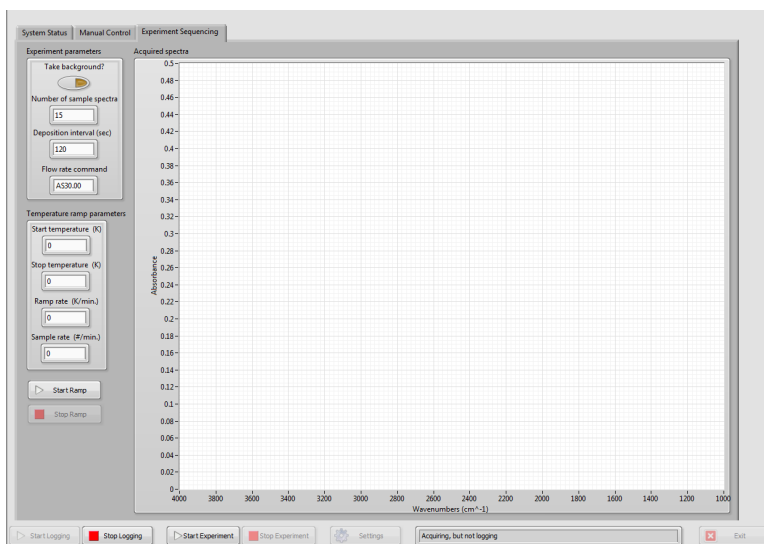
Figure 15: Experimental setup display for the Labview code with the default parameters for number of samples to collect, deposition time, and flow rate for the neon.

2. **Deposition Time** 120 seconds

3. **Flow Rate Command** 40 sccm

The next main function of the Experimental Sequencing window is the ability to set a temperature ramp for the window. This should be used after every experiment takes place to ensure that the window is clean for the next experiment. The user will set a start temperature (likely the current temp), the stop temperature, and the rate to increase the heat. Note, the user can also manually ramp the heat by turning on the "Heat Ramp Power Supply" and slowly increasing the voltage levels.

OMNIC OMNIC is the software that comes standard with the FTIR device. It is a Graphical User Interface that allows the user to manipulate the controls of the FTIR directly, and visualize the spectrum the the FTIR collects. Since OMNIC and the Labview program are connected, the user only needs to develop the experimental setup, and collect and save the background. Everything else is taken care of by the Labview code. the GUI for OMNIC is shown in Figure 16

Prior to taking data, it is important to set up OMNIC specifically for the experiment. To do this, click the "Expt Set" button located in the top left corner. This will open a window with various tabs, the first being "collect." From top to bottom, the first setting the user can change is the "number of scans." This is the number of times the FTIR scans the sample and returns an
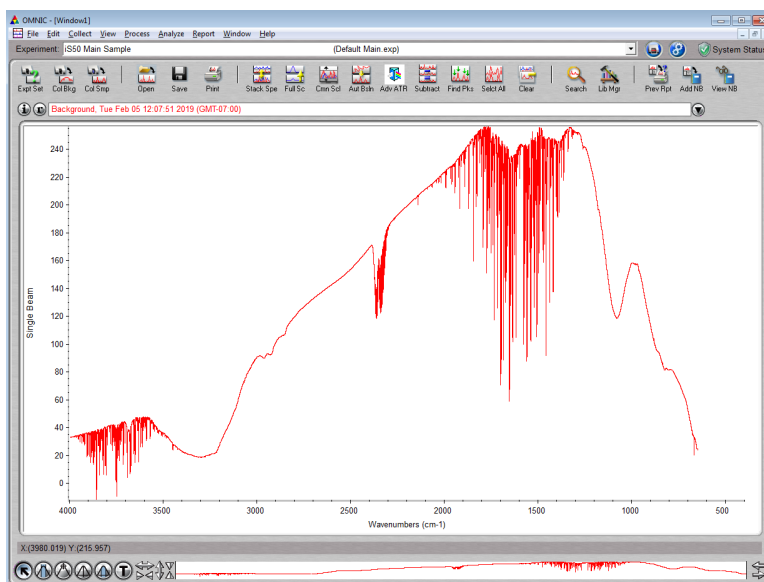
Figure 16: Main display of OMNIC, the standard software for the FTIR with a sample background.

overall average. The next parameter is "resolution." This setting allows you to change the spectral resolution, which determines how close two peaks can be and still be identified as separate peaks. Smaller resolution numbers generally equate to better spectral lines, however there are always trade offs. Higher resolution (smaller numerical values) will take longer to for the system to collect, and increases the noise. Because of this, it is generally best to set the resolution only as high as needed to differentiate between individual peaks. The only other setting under the "collect" tab that is frequently altered are the radio buttons under "Background Handling." This allows the user to specify when to collect a spectral image of the background, when no sample is present. Because the system works in conjunction with the Labview software, it is important to select "Collect background after" and choose a time much greater than the experiment will run for. An image of the default selection criteria for the experiment is shown in Figure 17.

While still inside the Experimental Setup window, the next tab that is commonly used is labeled, "Bench." This tab displays a live image of the interferogram, which gives a visual cue to what the detector's signal is. Before conducting an experiment, or anytime the FTIR's cavity has been moved away from the cryogenic chamber, the system must be manually aligned. To do this, the user must manipulate the FTIR into position while observing the interferogram and min/max values listed. The user should strive for a min/max value of ± 10, with an interferogram that resembles the one in figure 18.
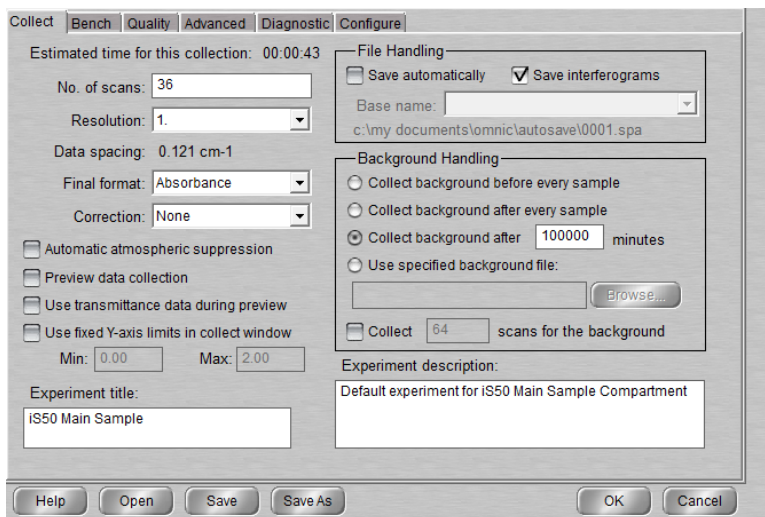
Figure 17: OMNIC experimental setup, collection page given with default parameters for experiment.

Figure 18: OMNIC experimental setup, bench page given with default parameters for experiment and proper interferogram depiction.

4.2 Full Experimental Procedures

This section outlines the full procedures to run an experiment from start to finish. Prior to running an experiment, the system must be pumped down to at least $1*10^{-7}$ Torr, and the window temperature should be resting at approximately 5.5K.

1. Locate the main water manifold in the service corridor. On this manifold, ensure the return and supply valves to the Quanta-Ray laser are open.

2. Turn on the FTIR and fill the MCT reservoir with liquid nitrogen until full. This system should cool for at least 15 minutes before taking a background scan.

3. Turn the laser setting to "LP" (long pulse) and turn on. Allow the laser to simmer and increase the laser oscillatory knob until the pulse can be seen. Take caution to avoid eye exposure to the beam. Align the beam to the top-left section of the target by manipulating the dials on the mirror-mounted motor driver. Once aligned, turn the oscillatory knob to zero.

4. Add in descants to help reduce water noise, fit the background isolation box over the FTIR and purge with nitrogen. The nitrogen line should be open fully to purge the background of unwanted water and carbon dioxide molecules. The system should purge for at least 15 minutes before running an experiment.

5. Open OMNIC and enter experiment parameters under experimental setup. Select the "Bench" tab and manually align the FTIR until the interferogram shows the expected results.

6. Set a power meter into the empty post-holder along the beam path. Ensure the power meter is set to the proper wavelength of 532nm and the beam path is properly covered to avoid eye exposure. Turn the Quanta-Ray Nd:YAG laser to the "Q-switch" setting, and turn the oscillatory knob up, observing the power meter, until a desired power is reached.

7. Turn on the motor-driver and shield power supply. Check the power meter and ensure the it has dropped to zero, which shows the shield is blocking the laser. While wearing protective eye-wear, open the cover to the beam path and remove the power meter.

8. Open the valves on both the Neon and Hydrogen regulators.

9. Using OMNIC, collect a background scan. If the scan appears to be too noisy, wait five minutes and attempt again. Once a background is collected, save the background as both a .spa and .csv file to the desktop of the computer.

10. In the Labview program, setup the experiment by entering the number of samples to collect, the deposition time, and the flow for the neon.

11. Select "Begin Experiment" on the Labview program and monitor results.

12. Monitor the following to ensure best results:

    - To ensure the motor driver is moving the mirror mount, watch for orange and blue light emitting diodes that illuminate during the ablation process.
    - The Alicat mass flow controller that regulates Neon flow should drop to 0.0sccm when the laser is shielded.
    - Monitor pressure and temperature on the Labview program. The pressure should depict a square-wave pattern from the regulation of the neon.

13. After the experiment is completed, turn the laser oscillatory knob to zero, and follow the reverse steps to set everything in a standby mode.

14. Prior to conducting another experiment, the window must be cleaned by heating the window holder. This can either be done manually by slowly increasing the voltage on the power supply for the window temperature or by using the Labview software.

4.3   Experimental Process

The process for the experiment is cyclic and can run as many times as the user desires. It begins with the pulsed laser. The laser is created using the Nd:YAG crystal, or neodymium-doped yttrium aluminum garnet, $Nd : Y_3Al_5O_{12}$. It commonly has a fundamental frequency of 1064nm but can use a doubling crystal to create the second or third harmonic, 532nm and 355nm respectfully. This experiment utilizes the 532nm harmonic, which after exiting the laser head is directed along a series of mirrors called the beam path. Along this path, the beam strikes a mirror that is mounted onto a motor driver. This motor driver constantly moves the mirror so the beam traverses the target in a serpentine pattern from top-left to bottom-right. This ensures the target does not become pitted during the ablation process. Before entering the cryogenic chamber, the laser passes through a 400mm Plano-Convex lens, which focuses the beam to a minimal spot size. When the laser beam strikes the target with sufficient energy, particles from the surface of the solid target become a plume of thermalized, gaseous plasma. The beam path is depicted in Figure 19, and an actual image of my setup along with the ablation process is shown in Figure 20.

Concurrently, neon and hydrogen gas enter the buffer gas cell from two separate flow controllers. To ensure the hydrogen does not freeze, a resistive wire heating element was added to its tube, then wrapped in Kapton tape and Mylar to avoid heating the widow post. The gases enter the chamber and mix with the ablated plasma. This plume is then forced out of the small aperture at the bottom of the cell in a mixture called the molecular beam. This molecular beam strikes the window then quickly freezes, trapping the carbon-hydrogen molecules in a matrix made of neon host molecules.
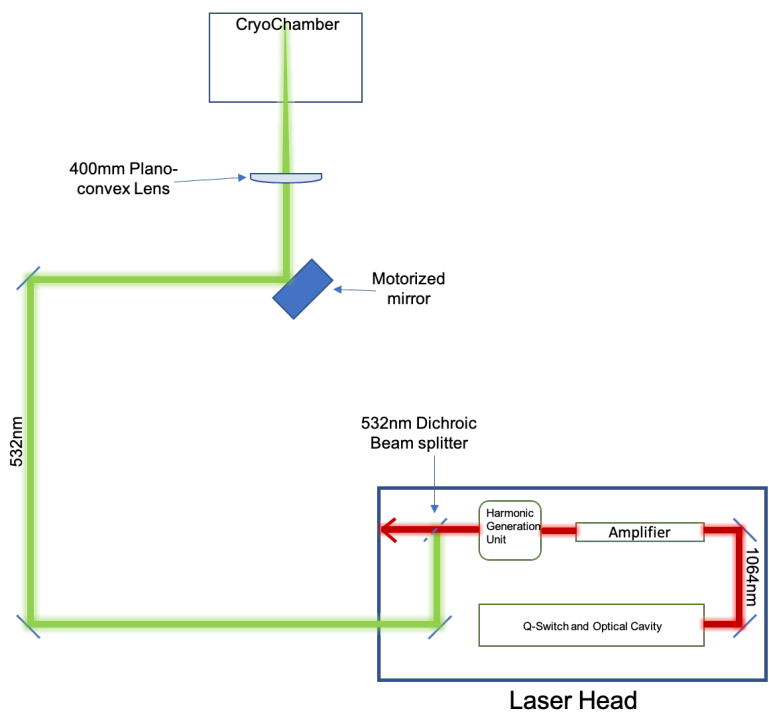
Figure 19: Diagram for the beam path. The beam starts at the laser head with a fundamental frequency of 1064nm. After passing through a harmonic generation unit, the second harmonic is peeled off and sent the the chamber for the ablation process.
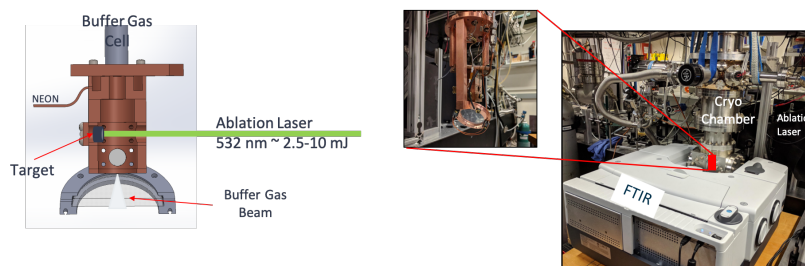
Figure 20: Image showing my experimental setup (right) and how the FTIR wraps around the cryo-chamber. The image on the left depicts how the laser ablation occurs to create the buffer gas beam.

After the deposition time elapses, the ablation from the Nd:YAG laser stops, the neon flow subsides, and the FTIR begins scanning through the window. The scanning time period depends on the number of scans that it averages and the resolution that the user inputs prior to the experiment. It scans across a broad spectrum, exciting any molecules that absorb the frequency resonant with their vibrational modes. After the scan process finishes, OMNIC outputs the spectral absorption onto its GUI, and the process starts over again.

The importance of taking multiple scans is to confirm that a specific molecule is created during the ablation process. Each molecular beam that is frozen on the window creates a layer of trapped molecules that will increase the absorption from the FTIR's scan. It is expected that if the same molecule is consistently created during each ablation process, then the peaks that arise from absorption will grow in linearly, confirming the molecule created.

5   Results

My experiment includes three general results: the carbon cluster recreation experiment, the simulation of the buffer gas cell using COMSOL Multipysics, and finally, the capture and creation of hydrocarbons in matrix isolation. Details of each are given in the sections below.

5.1   Carbon Cluster Tests

In 2017, Dr. Cameron Straatsma conducted an experiment using the buffer gas cell with matrix isolation to study the formation of carbon clusters from an ablated source. Since my experiment, the study of hydrocarbons in matrix isolation, closely mirrored Dr. Straatsma's, I intended to recreate his carbon cluster experiment before adding hydrogen to the source. Conducting this experiment first offered three advantages before attempting the observation of hydrocarbons. First, similar results would ensure my system was set up correctly and working properly. Next, it allowed me to gain experience in vibrational spectroscopy with known results, and finally, it allowed me to confirm and narrow down carbon cluster vibrational modes from previously published data.

After conducting the experiment, using the same methods as Dr. Straatsma and as outlined in the methods section, excluding the introduction of a hydrogen source, my observations were very similar to the published results. I observed large peaks with similar ratios at all the demonstrated carbon cluster vibrational modes as predicted and demonstrated by Dr. Straastma, which is shown in Figure 21.

Note, in Figure 21, Dr. Straatsma uses the value "Optical Depth" to indicate the absorbance from the molecule while my analysis was found in "Absorbance". Here, "Optical" Depth is found via Beer's Law as described by 3.1.23 and "Absorbance" is defined by 3.1.22. Optical Depth can easily be converted to absorbance, as shown:
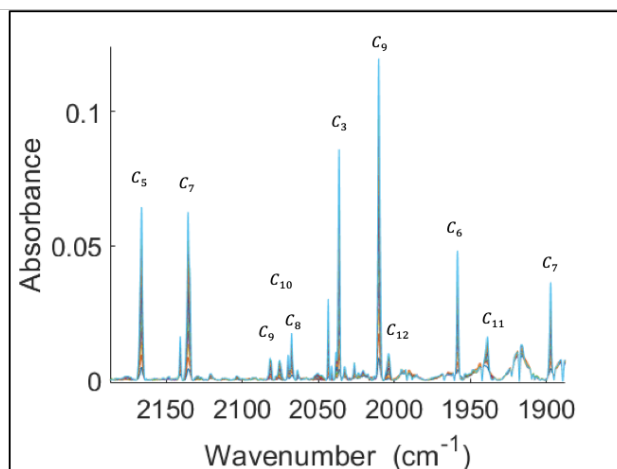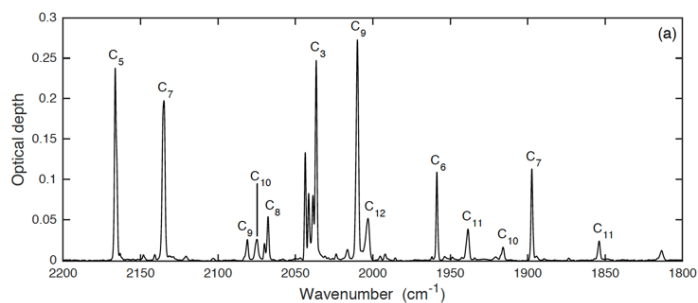
Figure 21: Carbon cluster data collected and analyzed by Dr. Cameron Straatsma (top) compared to my results from recreating that experiment (bottom). Data from my experiment closely lines up to Dr. Straatsma's and shows all peaks with similar ratios.
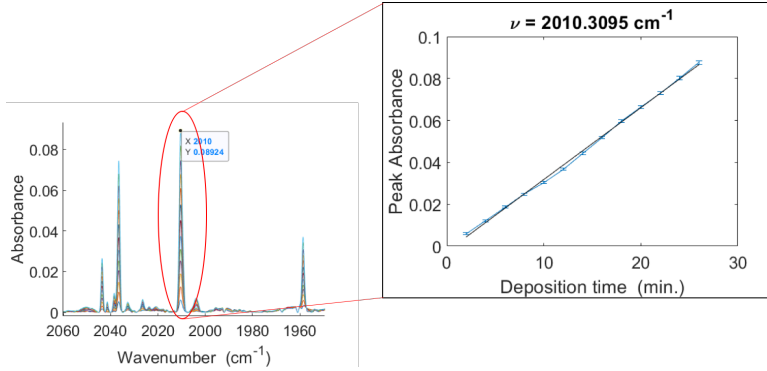
Figure 22: Image showing the growth trend of the large carbon cluster peak at $2010 cm^{-1}$, comparing the deposition time versus absorbance. Based on the fact that the laser pulse energies are consistent with a consistent neon flow rate, a linear growth is expected and observed.

$$\tau = ln(\frac{\Phi_I}{\Phi_T}) \tag{5.1.1}$$

$$e^\tau = \frac{\Phi_I}{\Phi_T} \tag{5.1.2}$$

$$-Log_{10}(e^{-\tau}) = -Log_{10}(\frac{\Phi_T}{\Phi_I}) = A \tag{5.1.3}$$

Here, Φ_I is the incident flux of light, Φ_T is the transmitted flux of light and τ is the optical depth.

Since the laser energy per pulse tends to be consistent, and the neon flow is set to consistent parameters, a linear growth is expected over the course of 10-15 cycles of deposition. Figure 22 shows the growth of one of the carbon clusters over time, as well as the fit, which shows linear progression as expected.

5.2 Simulation of Fluid Dynamics

When I began working with buffer gases and molecular beams, I wanted to understand more about the fluid mechanics and dynamics of the neon flow inside the chamber. Analysis on this would help determine the best flow rate to maximize production and gain insight to the flow of the buffer gas.

For the simulation, I used a program called COMSOL multiphysics and modeled it in the molecular flow regime, with a Knudsen number of approximately 10. I had to create an inverse model of my buffer gas cell, filling the void spaces as a solid as required by the program. The input parameters, besides the temperature and pressure, are the molecular weight of neon, $0.02018\frac{kg}{mol}$ and the outgoing flux, which is determined by the flow rate of neon, which is a parameter I can control, and the mean molecular velocity of neon, given as
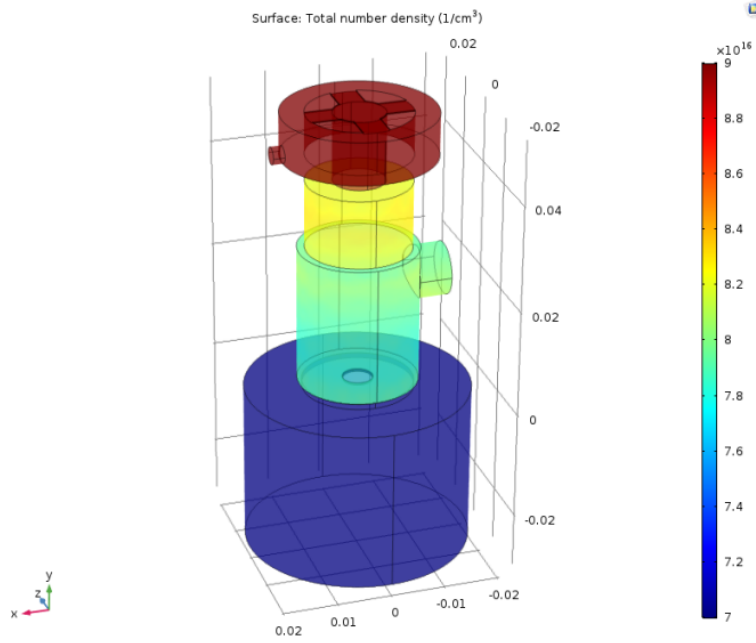
Figure 23: Simulation of the Buffer Gas Cell's number density for flowing Neon in at a rate of 100 sccm.

$$\bar{v} = \sqrt{\frac{3kT}{m}} \qquad (5.2.1)$$

Here, k is the Boltzmann constant, T is the temperature, and m is the mass. With the given parameters, the simulations give an approximate value of $8 * 10^{16} cm^{-3}$ for the number density with a flow rate set to 100sccm, as shown in the Figure 24.

To test if this simulation is accurate, I can make a very approximated calculation of my proposed number density by exploiting the fact that at 1 STP, $4.47796 * 10^{17} \frac{N}{s} = 1 \frac{cm^3}{min} (sccm)$, which is helpful since I can control standard cubic-centimeters per minute, or sccm. Using this, I can approximate the number density with the following equation

$$n_{neon}(sccm) = \frac{4.47796 * 10^{17} \frac{N}{s} * f[sccm]}{\bar{v} * A} \qquad (5.2.2)$$

where A is the area and $\bar{v}$ is the mean molecular velocity of neon. Plotting the approximation as a function of flow rate against the simulated values gives the comparison in figure 24.

As another check to determine the validity of the simulation, I compared the simulated result against documented values of the number density of neon

37
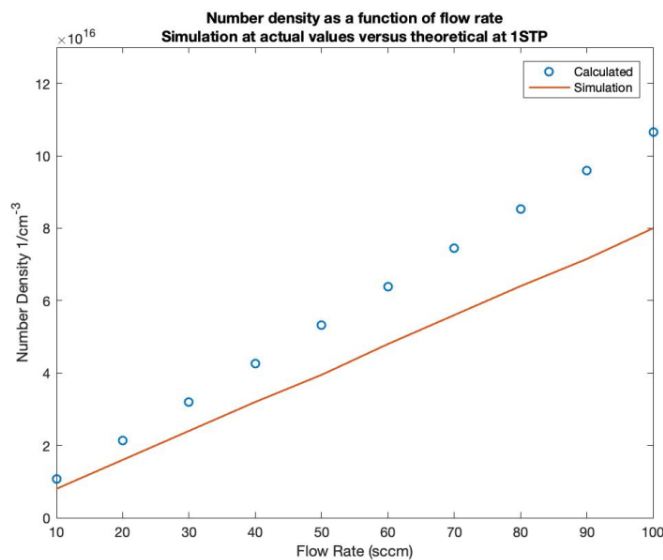
Figure 24: Comparison of flowrate versus number density pitting the calculated approximation (blue circles) against the simulation (red).

in a buffer gas cell. A PhD. thesis from Harvard University gave results for the number density of neon inside a buffer gas cell with similar dimensions as mine, with a value of $3 * 10^{16} \frac{1}{cm^3}$ [3].

5.3 Hydrocarbon Observation in Matrix Isolation

5.3.1 Trapping Methane in Matrix Isolation using a Buffer Gas Source

The observations of Hydrocarbons in matrix isolation, with the hopes of observing methylidyne, was the primary goal of this experiment. To conduct this, our concept was to bleed hydrogen into the buffer gas cell during the ablation process in hopes to create hydrocarbon bonds from the resulting plasma. Issues began to arise with the freezing temperature of hydrogen being at 14K and the fact that hydrogen, having one of the fastest molecular velocities, is difficult to pump. With these issues, I decided to first capture a hydrocarbon in a matrix to test the plausibility of the idea. I did this by adding methane instead of hydrogen to buffer gas cell. Methane freezes at 91K, and I had to heat the line that enters the buffer gas cell to ensure methane would reach the target. To do this, I wrapped the tube in 236 centimeters of nichrome wire with a resistance of $0.346 \frac{\Omega}{cm}$ and attached it to a power supply. I then covered the wire with kapton tape and mylar shielding to help disperse the heat produced away from the window where the matrix isolation occurs. I then pumped in

38
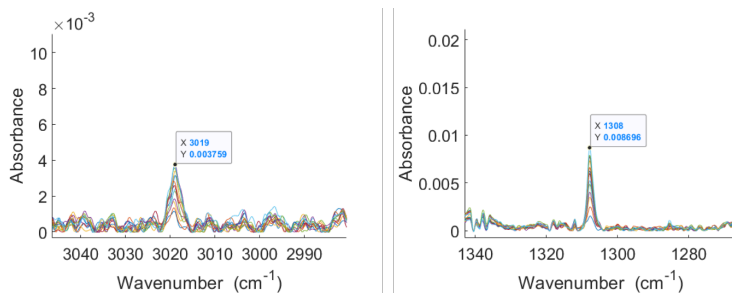
Figure 25: After the introduction of methane gas into the buffer gas cell, I observed the hydrocarbon trapped in an isolated matrix given by the two vibrational modes 1308 and $3019 cm^{-1}$.

methane while supplying the nichrome wire with $15V$ to heat the tube. This allowed the methane to pass through the tube into the buffer gas cell where it then froze on the inner walls and graphite target. I then ran the experiment as outlined in the Methods section of this thesis and observed new vibrational modes at $1308 cm^{-1}$ and $3019 cm^{-1}$, which can be seen in Figure 25. 1308 and 3019 are both well documented vibrational modes of methane, which correspond to asymmetric stretches and deformations respectively.

To ensure the resultant vibrational modes were in fact methane that was frozen on my target and subsequently ablated with the graphite, I warmed the matrix isolation window to 50K, below the freezing point of methane, but warm enough to clean the window from all other sources and ran the experiment again without the laser ablation. This resulted in the peaks at 1308 and $3019 cm^{-1}$ remaining, but with no growth. This told me that the molecule remained on the window after the warming process and that it only accumulated during laser ablation. I ran the experiment again and once again observed growth in the 1308 and $3010 cm^{-1}$ wavenumbers. However, the growth was not linear, and instead began to taper off with each subsequent ablation process as shown in Figure 26. This confirmed that the molecule was on the target during the ablation process and, since the methane was not continuously pumped into the chamber during ablation, the decaying growth was expected.

Finally, to confirm this was in fact methane and not another molecule, I warmed the window to room temperature which would have cleaned the window and buffer gas cell of all methane. After cooling the chamber, I ran the experiment again with no introduction of methane to the system. The peaks from 1308 and $3019 cm^{-1}$ disappeared completely, confirming that I had trapped a hydrocarbon in matrix isolation using a buffer gas beam.

5.3.2 Creation of Hydrocarbons Using a Buffer Gas Source

To ensure accurate, consistent results, I first had to characterize the hydrogen line that sourced the hydrogen to the buffer gas cell. This was important for
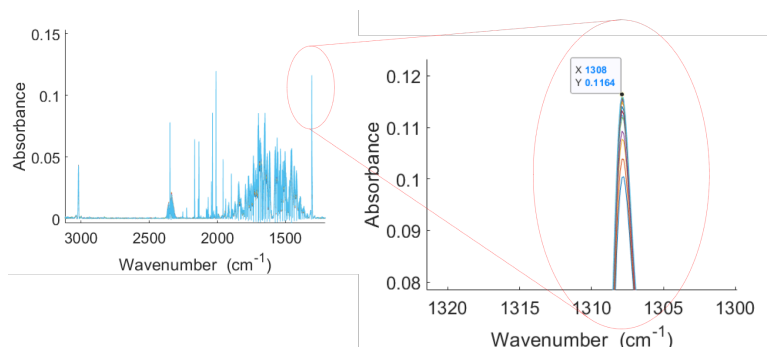
Figure 26: $1308cm^{-1}$ vibrational mode of methane after warming the window to 50K and running the experiment again. The growth of each successive deposition decays as expected, confirming the methane was coated on the graphite target

two reasons: I had to keep the window as cold as possible to ensure maximum deposition, and I needed a consistent hydrogen flow into the buffer gas chamber to see linear growth. I characterized it by changing the voltage levels that supplied current to the nichrome heating wire, then flowed hydrogen into the line. If the pressure reading from the ion gauge increased, then hydrogen was getting into the system. I found that the voltage power supply had to be at approximately $2V$ to heat the line sufficiently to allow hydrogen to flow while keeping the temperature change to a minimum.

With the line characterized, I ran the experiment as outlined in the methods section while changing various parameters. Finally, I found optimal flow rates and laser pulse energies that was conducive for making hydrocarbons. The experimental parameters are as follows:

- Laser Energy $\geq$ 8mJ

- Neon Flow: 37 $\frac{cm^3}{min}$

- Hydrogen flow: 0.05 $\frac{cm^3}{min}$

- Deposition time: 120s

When running the experiment with these parameters, I discovered new peaks at 3338, 3334, 3326, 3322, 3319, 2141 and a cluster around $3279cm^{-1}$ in the higher wave number regions. Figure 27 shows the new vibrational modes discovered at this region. After further analysis, I noticed small peaks grown in linearly near the 1235 region. These peaks include 1246, 1245, 1242, 1236, and $1233cm^{-1}$, and an image of them can be seen in Figure 28.

One important observation during this experiment was the dependence of laser energy. My first observation of hydrocarbons came after fixing the hydrogen intake valve and setting the laser to 4mJ/pulse, which showed vibrational
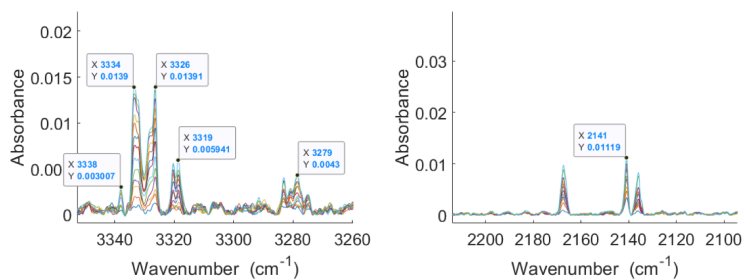
Figure 27: Vibrational modes excited during the experimental process after adding in hydrogen to an ablated carbon source. The 3334 and $2141 cm^{-1}$ peaks correspond to Propyne, C_3H_4, and the others are likely hydrocarbons.
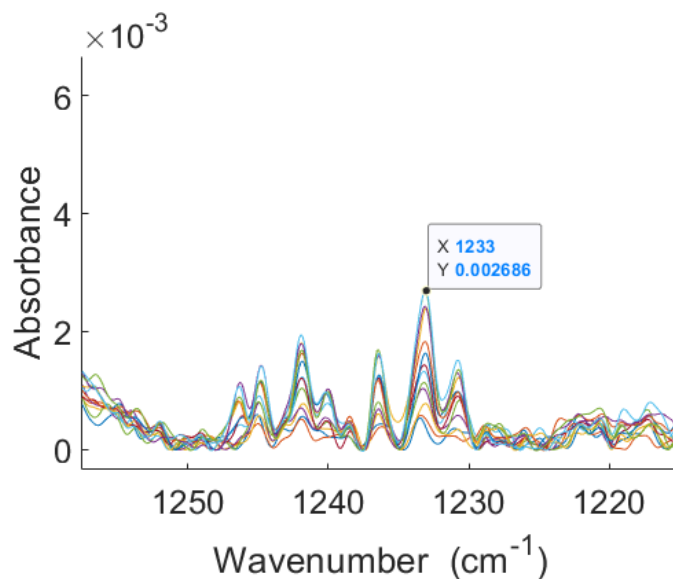
Figure 28: Vibrational modes excited during the experimental process after adding in hydrogen to an ablated carbon source near the $1233 cm^{-1}$ region. These vibrational modes could possibly correspond to C_3H_5 and C_4H_4. C_3H_5 has known C-H and mixed stretches at 1230, 1232, 1242, and $1245 cm^{-1}$, while C_4H_4 has know vibrational modes at approximately $1244 cm^{-1}$.
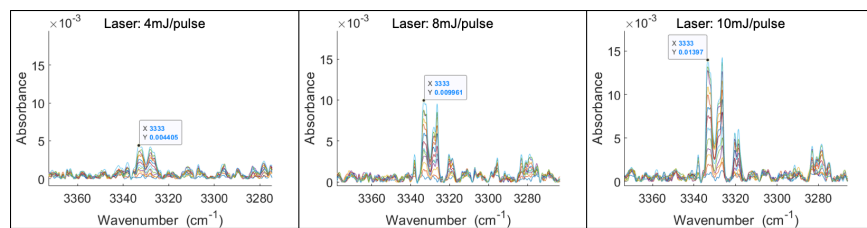
Figure 29: Vibrational modes excited during the experimental process after adding in hydrogen to an ablated carbon source. The increase in laser energies per pulse show a dramatic increase in the production of the hydrocarbons.

modes at $3333cm^{-1}$ and $3326cm^{-1}$ with an absorbance of 0.05. After increasing the laser energy from 4mJ/pulse to 8mJ/pulse, I observed new peaks of hydrocarbons, generally clustering around $3333cm^{-1}$, with a max absorbance peak of 0.01, doubling the 4mJ/pulse observations. Finally, I ran the experiment again, increasing the laser energy to 10mJ/pulse and saw an increase in all peaks by approximately 50%. The newly observed peaks, and the relative laser energies can be seen in Figure 29.

After conducting research into known vibrational nodes for hydrocarbons using the NIST webbook [11], it is likely the peaks at 3334 and $2141cm^{-1}$ correspond to the molecule propyne, C_3H_4. This molecule has well documented vibrational modes at these wavenumbers, where the 3334 vibrational mode corresponds to the C-H stretch and the $2141cm^{-1}$ corresponds to a C-C stretch, triple bond. The other stretches that encircle this are likely C_3H_3 at $3326cm^{-1}$ and C_3H_2 at $3283cm^{-1}$, both of which are well documented, and since C_3 is a high producing carbon cluster, it is likely creating a hydrocarbon of the same order of carbon. Other likely candidates include C_4H_2 and C_5H, both of which have known vibrational modes in this region. On the other side of the spectrum, near $1233cm^{-1}$, likely hydrocarbons are C_3H_5 and C_4H_4. C_3H_5 has known C-H and mixed stretches at 1230, 1232, 1242, and $1245cm^{-1}$, all of which are observed peaks. This also corresponds well with my hypothesis that if I was making a number of C_3 clusters, I would see hydrocarbons with C_3 bonds.

6 Future Projections and Conclusion

Science is an ongoing project, where each step progresses human-kind to a better tomorrow. My experiment is no different, since I picked up where someone left off, and, hopefully I will pass the torch to another. While I succeeded in finding and creating hydrocarbons, the next step of the experiment is to create the C-H radical, or methylidyne, using a buffer gas cell and molecular beam. One possible method to do this is to increase the power of the laser, since, as I have shown, the production of hydrocarbons is a function of laser pulse energies. However, to successfully increase the laser energies per pulse, care is needed not to destroy equipment. Previously, with an increase in the energy per pulse, the laser burned holes in the windows of both the cryogenic chamber and the buffer gas cell. To avoid this kind of damage, the next user could possibly replace the current, 400mm plano-convex lens with a faster one and place it inside the cryogenic chamber. This would ensure the beam is at full diameter when entering the first window, and still decreasing to a minimal spot size before entering the buffer gas cell, which may allow the user to safely increase the laser energies per pulse. However, this would be an invasive and difficult task that would likely require the realignment of mirrors, changing the parameters on the motorized mirror mount, and finding a way to fasten the new lens inside the chamber.

Another interesting experiment would be to determine how the flow of hydrogen affects the production of the hydrocarbons. Most of my early failures with the creation of hydrocarbons were possibly due to the fact that I was setting the hydrogen flow rate too high. After I attempted lower rates, specifically 0.05sccm, I saw the signal that I was looking for. This was likely due to the difficulties of pumping hydrogen, which will cause my window to heat as the pressure spikes, amounting to a loss in signal. However, now that I have found a good flow rate that produces hydrocarbons, one could hold all parameters fixed while varying this one, to see how it effects the production rate.

Overall, I accomplished what I set out to do: I created hydrocarbons inside a buffer gas cell and used a molecular beam to trap them inside an isolate matrix. The culmination of this experiment over the last couple years has been as rewarding as the experiment was challenging. It taught me a lot about the field of physics and the subfields of spectroscopy, quantum mechanics, and molecular chemistry, and I am ever grateful for the opportunity to have been part of it.

References

[1] Andrews, Lester, and Martin Moskovits. *Chemistry and Physics of Matrix-Isolated Species.* North-Holland, 1989.

[2] Atkins, P. W., and Ronald Friedman. *Molecular Quantum Mechanics.* Second ed., Oxford University Press, 1983.

[3] Egorov, Dimitri Michael. Buffer-Gas Cooling of Diatomic Molecules. *Harvard University,* Dimitri Michael Egorov, 2004, pp. 3234.

[4] Griffiths, Peter R., and De Haseth James A. *Fourier Transform Infrared Spectrometry.* Wiley-Interscience, 2007.

[5] Hutzler, Nicholas R., et al. The Buffer Gas Beam: An Intense, Cold, and Slow Source for Atoms and Molecules. *Chemical Reviews,* , vol. 112, no. 9, 2012, pp. 48034827., doi:10.1021/cr200362u.

[6] Jarrett, Max. Lights out: poor governance and Africas energy crisis, http://www.theafricareport.com/News-Analysis/lights-out-africas.html.

[7] Lira, Carl. Brief History of the Steam Engine. *Steam Engine History,* 1994, www.egr.msu.edu/ lira/supp/steam/.

[8] McIntyre, David H., et al. *Quantum Mechanics.* Pearson, 2016.

[9] Mobley, Benjamin *The Cryogenic Buffer Gas Beam and the Spectroscopy of Carbon Clusters.* The University of Colorado - Boulder. 2017.

[10] Moran, Craig. Australia Energy Market. *Lessons From Australia's Energy Crisis.* www.worldpolicy.org/2017/04/04/lessons-from-australias-energy-crisis/

[11] NIST Chemistry WebBook, SRD 69. (n.d.). Retrieved from https://webbook.nist.gov/chemistry/vib-ser/

[12] Orville-Thomas, W. J. The History of Matrix Isolation Spectroscopy. *Matrix Isolation Spectroscopy,* 1981, pp. 111., $doi : 10.1007/978 - 94 - 009 - 8540 - 7_1$.

[13] Pidd, Helen. India blackouts leave 700 million without power, 2012, www.theguardian.com/world/2012/jul/31/india-blackout-electricity-power-cuts.

[14] Ristinen, Robert A., et al. *Energy and Environment* Third ed., Wiley, 2016.

[15] Sjodin, Bjorn. What Is Molecular Flow? *COMSOL Multiphysics,* 2013, www.comsol.com/blogs/what-is-molecular-flow/.

[16] Taylor, John Robert. *Classical Mechanics.* University Science Books, 2005.